AGU PUBLICATIONS

JGR

Journal of Geophysical Research: Solid Earth

RESEARCH ARTICLE
10.1002/2017JB014633

Special Section:
Rock Physics of the Upper Crust

Shear Modulus Dispersion in Cracked and Fluid-Saturated Quartzites: Experimental Observations and Modeling

Heather Schijns[1,2], Ian Jackson[3], and Douglas R. Schmitt[1,4]

[1]Institute for Geophysical Research, Department of Physics, University of Alberta, Edmonton, Alberta, Canada, [2]Now at BHP, Perth, Western Australia, Australia, [3]Research School of Earth Sciences, Australian National University, Canberra, ACT, Australia, [4]Now at Earth, Atmospheric, and Planetary Sciences Department, Purdue University, West Lafayette, IN, USA

Key Points:
- Water saturation of the thermally cracked quartzites is experimentally observed to cause strong shear modulus dispersion between seismic and ultrasonic frequencies
- A mean crack aspect ratio of ~0.001 is inferred from the magnitude of the shear modulus deficit and the pressure dependence of the shear moduli
- Thermal cracking of essentially monomineralic quartzites induces substantial crack densities approaching 0.5 at low differential pressures

Supporting Information:
- Supporting Information S1

Correspondence to:
H. Schijns,
schijns@ualberta.net

Citation:
Schijns, H., Jackson, I., & Schmitt, D. R. (2018). Shear modulus dispersion in cracked and fluid-saturated quartzites: Experimental observations and modeling. *Journal of Geophysical Research: Solid Earth*, *123*, 2825–2840. https://doi.org/10.1002/2017JB014633

Received 29 JUN 2017
Accepted 2 FEB 2018
Accepted article online 8 FEB 2018
Published online 13 APR 2018

Abstract The effect of pore fluids on acoustic wave dispersion in rocks with low aspect ratio crack porosity is important for the interpretation of laboratory and field observations in hard rock mineral exploration environments. Here we make laboratory measurements of shear modulus dispersion at frequencies 0.01–1 Hz and at 1 MHz with different saturating fluids (dry, argon, and water saturated) in two thermally cracked quartzite samples with ~2% total porosity. Measurements are made across a range of effective pressures (10–150 MPa), with the resulting very low permeabilities of the samples varying from $1–300 \times 10^{-21}$ m^2. Moduli across the 0.01–1 Hz band were typically independent of frequency. The shear moduli measured at sub-Hz frequencies are unaffected by fluid saturation, as expected for the saturated isobaric (Gassmann) regime. In marked contrast, water saturation of the cracked rocks results in very large increases in the shear moduli measured at 1 MHz and low effective pressures, indicative of saturated isolated conditions. Thus, at an effective pressure of 20 MPa, the shear moduli for the two water-saturated quartzites increase by 74% and 98% from 1 Hz to 1 MHz. The contrast in elastic moduli between dry and water-saturated conditions is well represented by the theoretical model developed by Walsh and others. The observed dispersion highlights the need for care in seismological application of results obtained at MHz frequencies from laboratory ultrasonic measurements.

1. Introduction

Seismic methods are among the principal tools used in oil and gas exploration and are commonly used in environmental and engineering studies. Increasingly, the applicability of seismic methods in other areas, such as CO_2 sequestration monitoring and mineral exploration, is being investigated. Numerical modeling of rock acoustic properties can give an indication of the likelihood of successfully imaging subsurface features that have not historically been targeted by active surface seismic surveys. One issue with this is, however, that the seismic properties input to these models are typically obtained from laboratory (at MHz frequencies) or borehole measurements (at kHz frequencies) which may differ from field studies (typically 1–300 Hz) because of frequency-dependent velocity dispersion effects.

For example, relatively incompressible pore fluids capable of stress-induced flow between pores and cracks should result in a stiffening of the effective elastic moduli of the saturated rocks at higher frequencies, when the timescale of measurement is insufficient for fluid flow between pores and cracks so that they are hydraulically isolated. At lower frequencies, where pore fluids do have time to flow, the effective moduli should be lower due to the increased compliance of the saturated cracks. Numerous models have been developed to quantify the magnitude of velocity dispersion that can be expected between different frequency regimes and saturation conditions (e.g., Biot, 1956; Mavko & Jizba, 1991), but experimental measurements with which to constrain these are more limited, especially in cracked media.

Most studies to date have focused on rocks with higher porosities and more equant pores because of the implications of this dispersion for hydrocarbon exploration (e.g., Adam et al., 2009; Batzle et al., 2006; Pimienta et al., 2015; Spencer, 1981; Spencer & Shine, 2016; Tisato & Quintal, 2014; Winkler & Nur, 1982; Yin et al., 1992). The geometry of the porosity, however, has a significant effect on the amount of dispersion expected: the effect of spherical pores on the overall compressibility of the rock is proportional to the porosity, while bulk compressibility caused by low aspect ratio cracks is proportional to the rate of change of porosity with pressure. At low porosities equant pores have only a small effect on the total compressibility of rock and can therefore cause only limited dispersion while, even at low porosities, highly compressible

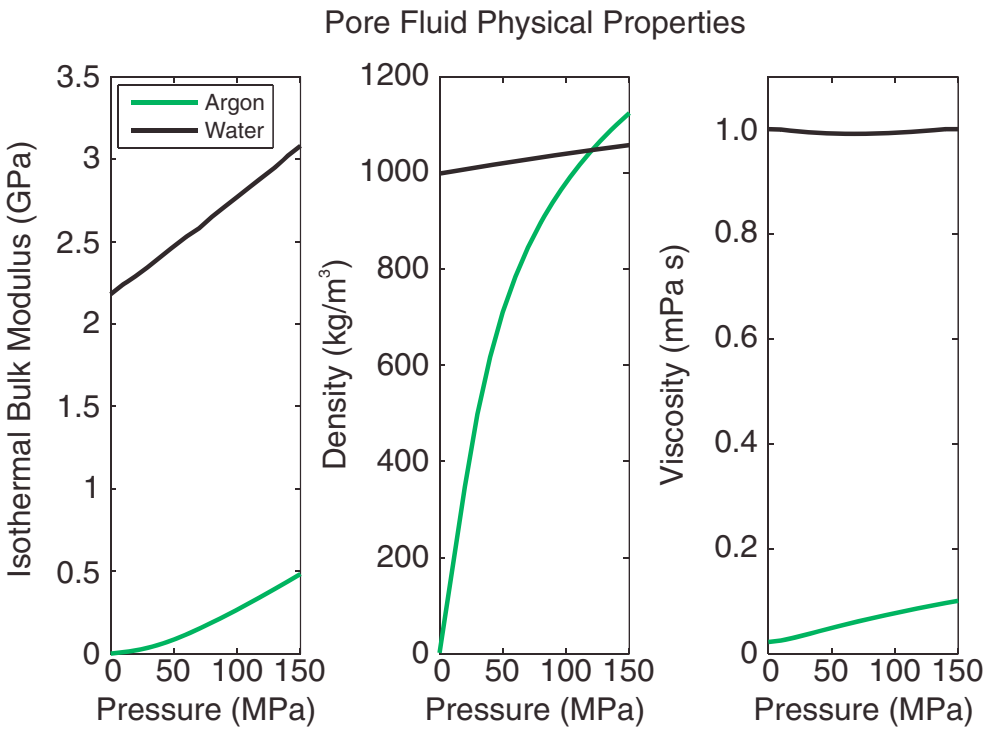

Figure 1. Physical properties of the argon and water used to saturate the quartzite samples. Values from National Institute of Standards and Technology (2012).

cracks can still significantly affect the bulk acoustic properties when given sufficient time to close (Walsh, 1965). This dependence of the moduli on the time frame of crack closure can result in dispersion in cracked rocks even at low porosities. As seismic methods become more commonly used in crystalline rocks (e.g., Chan & Schmitt, 2015; Hajnal et al., 2010; Heinonen et al., 2013; Koivisto et al., 2012; Malehmir et al., 2012; Milkereit et al., 1996; Schijns et al., 2009; White & Malinowski, 2012), which typically exhibit these low aspect ratio cracks, the importance of quantifying the dispersion caused by cracks increases (Sun et al., 2009). However, there have been very few direct experimental observations of dispersion in low-porosity rocks with low aspect ratio cracks. We therefore investigate the shear modulus dispersion displayed by two saturated, fractured, low-porosity quartzite specimens.

In this exploratory study, the shear moduli dispersion of cracked quartzite specimens from Cape Sorell, Australia, and Alberta, Canada, are measured over the frequency range of 0.01–1 Hz and at 1 MHz when the samples are dry, argon saturated, and water saturated. The mineralogy, grain sizes, and the thermally induced cracks in the quartzites are characterized; additionally, permeability is measured as a function of pressure for a comprehensive quantification of the properties of the quartzite. Dispersion measurements are made at effective confining pressures of 10–150 MPa to investigate the effects of crack closure.

2. Characterization of Rock Specimens

Two quartzite specimens, one from Cape Sorell, Tasmania, Australia, and one from Alberta, Canada, were selected for their relative homogeneity and near-monominerallic nature. Argon and water pore fluids were chosen for the dispersion study to allow observation of the effects of fluids with very different viscosities and bulk densities (Figure 1). In order to aid in understanding the effect of fluid-filled porosity on bulk elastic properties of the rock, it is necessary to characterize the matrix material as well as the shape, volume, and connectivity of the pore space as thoroughly as possible. The samples were characterized using scanning electron microscope (SEM), light microscopy on thin sections, mercury porosimetry, and, for the Alberta quartzite, X-ray diffraction. Permeability measurements as a function of pressure were also undertaken for both samples.

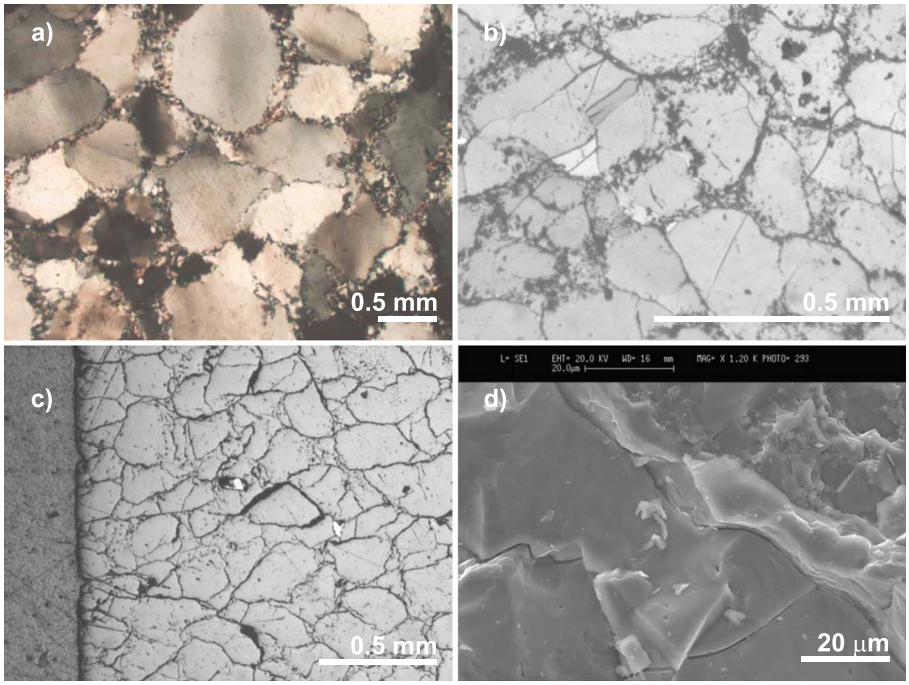

Figure 2. Thin section image of the Cape Sorell quartzite under transmitted light with cross-polarized filter prior to thermal cracking (a), with transmitted light after thermal cracking (b), with reflected light showing a cross section of the edge of the core sample after thermal cracking (c), and SEM image of the quartzite after thermal cracking (d). The muscovite at the grain boundaries is clearly seen in (a), while the relatively random distribution of cracks can be seen in (b) and (c).

Both quartzite specimens are dominated by quartz grains of ~0.5 mm diameter. The Cape Sorell specimen (Figure 2) is a translucent light gray in appearance and has been shown to be more than 99% quartz by volume, with $<$1% muscovite at the grain boundaries (Lu & Jackson, 1998). X-ray diffraction and SEM confirm that the Alberta quartzite, by comparison, is nearly entirely composed of quartz grains with a thin film of iron oxide at the grain boundaries (Figure 3). The appearance of the Alberta quartzite is largely controlled by the iron; initially the quartzite was an opaque brown-beige color, but upon heating the sample to induce crack porosity the quartzite changed to a pale pink color.

The bulk envelope volume of the quartzites is calculated from dimensional measurements made using vernier calipers on the thermally cracked, precision-ground samples. The sample mass and mercury porosimetry-measured porosity are used in conjunction with this measured envelope volume to calculate a grain density of 2,708 ± 7 kg/m^3 for the Cape Sorell quartzite; the Alberta sample is measured to have a grain density of 2,659 ± 7 kg/m^3. The Cape Sorell results are ~2% different to the density of 2,637 kg/m^3 measured by Lu and Jackson (1998) using Archimedes principle. This small discrepancy is likely indicative of local heterogeneity between the porosity or mineralogy of the Cape Sorell samples measured in the separate studies. Comparatively, Smyth and McCormick (1995) measure the X-ray density of pure quartz to be 2,648 kg/m^3, similar to the results for both quartzites. This again indicates that the quartzites are relatively pure, although the slightly higher grain densities measured in these quartzite samples may result from a small proportion of alternate minerals. The quartz-dominated mineralogy of the two samples simplifies comparison between experimental and theoretical results.

Thin section images of the quartzites prior to any treatment showed that they initially did not have significant crack porosity (Figures 2 and 3); saturating with distilled water in a vacuum gave an initial porosity of 0.3% in the Cape Sorell quartzite (Lu & Jackson, 1998), and mercury porosimetry measured 0.8% initial porosity in the Alberta quartzite. In order to increase the crack porosity and thereby the potential dispersion, it was necessary to induce additional cracks into these materials.

It is important to carefully consider the characteristics of the introduced cracks as their distributions and geometries have the potential to bias the observations. For example, the forced oscillation measurement of the shear modulus at low frequencies is particularly sensitive to cracks at the outer diameter of a

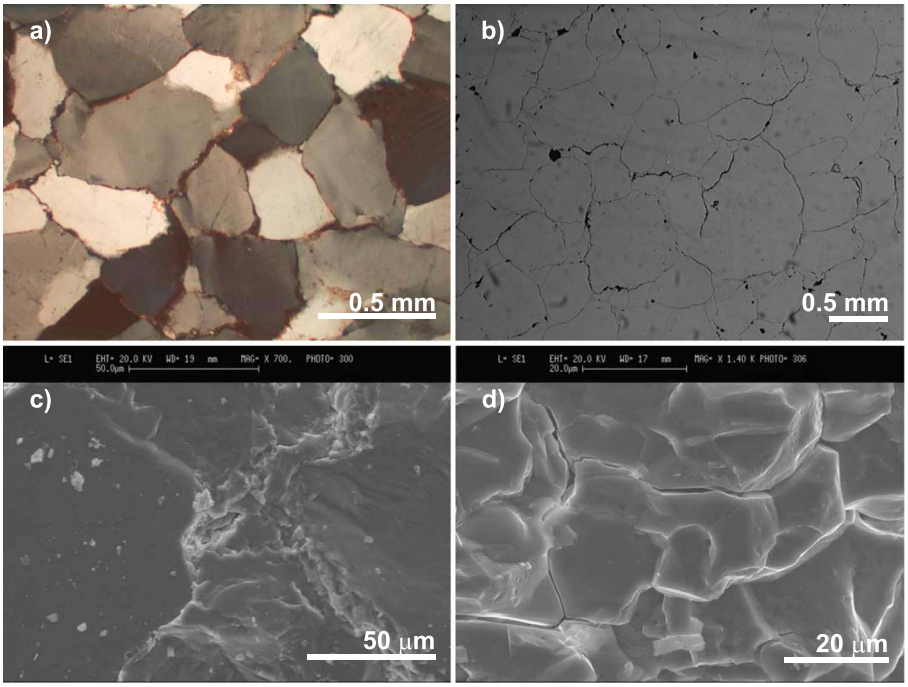

Figure 3. Alberta quartzite thin section prior to thermal cracking: with transmitted light and cross-polarized filter (a), reflected light (b), and an SEM image (c). The last panel shows an SEM image after thermal cracking (d). The iron oxide film at grain boundaries is particularly evident in (a), while the low aspect ratio nature of the cracks is highlighted in (d).

cylindrical sample, while the ultrasonic pulse transmission method used for the high-frequency measurement is more sensitive to cracks in the center of the sample. Comparison between measurements of the two frequency regimes would be further complicated by an anisotropic distribution of cracks. For these reasons, it was therefore desirable to induce within the quartzites as randomly oriented and homogeneous a crack distribution as possible.

Several combinations of temperature and quenching mechanism were investigated in this exploratory study to determine a methodology that produced sufficient crack porosity while maintaining the overall structural integrity of each sample. Test samples of 2.5 cm diameter and thickness of ~0.5 cm, prepared from the Alberta quartzite, were heated at a rate of 20°C/min to the target temperature, 1000°C, 1100°C, or 1400°C, where they were left to stabilize for ~3 h prior to quenching. Comparisons between quenching in liquid nitrogen and water were made on the specimens heated to 1000°C; these showed that quenching in room temperature water raised the porosity to 2.3%, while quenching in liquid nitrogen effected a total porosity of only 1.0%. Quenching from 1100°C into water created a porosity of 3.6% in the test piece, whereas the test sample heated to 1400°C lost structural integrity on quenching in water, cracking into multiple pieces. This led to a final decision to maximize the crack porosity while maintaining structural integrity by quenching the Alberta quartzite from 1100°C into water. As the mercury porosimetry is destructive, a separate sample had to be prepared for the dispersion experiment.

For the dispersion measurements, while the Alberta sample was cored at 2.5 cm diameter prior to undergoing heating and quenching, equipment restrictions required the sample to then be precision ground to a diameter of 1.5 cm and shortened from its original length of $>$15 cm. Crack porosity is anticipated to have resulted from the combined effect of thermal expansivity, the quartz α-β transition, and the quench. Of these, only thermal quenching is expected to produce heterogeneous or anisotropic results (Mallet et al., 2013). Due to the unforeseen necessity to reduce the Alberta quartzite sample diameter and length, the strongest effects of the quench may have been removed, as evidenced by the lower porosity measured in the quartzite used for the dispersion study, 2.4%; however, further investigation into this was not possible due to a lack of sample availability. While some anisotropy or heterogeneity may have remained in the crack distribution, characterization of such is beyond the scope of this exploratory study.

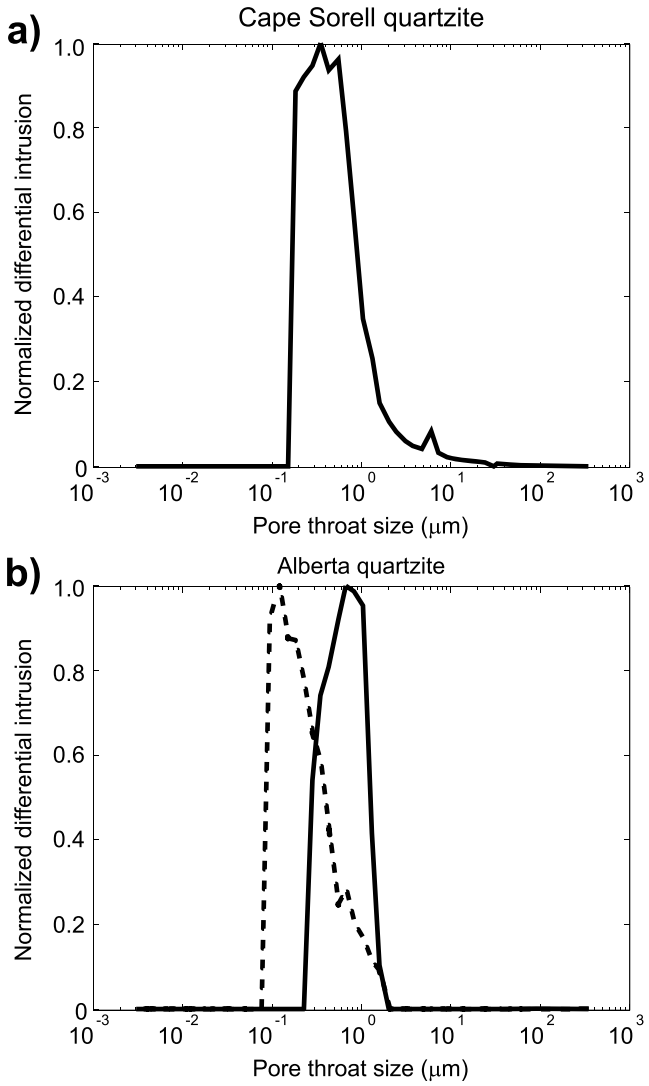

Figure 4. Mercury porosimetry of the (a) Cape Sorell and (b) Alberta quartzites showing that the cracks are sharply distributed around a single pore throat size for each quartzite, 0.4 and 0.7 μm, respectively. The dashed line in (b) shows the pore throat size distribution in an Alberta quartzite sample peaking at 0.1 μm prior to the induction of additional crack porosity.

The Cape Sorell quartzite was cored to the requisite 1.5 cm diameter and 5 cm length prior to heating to 1100°C and quenching, in this case, into liquid nitrogen. No sample-specific tests were carried out to determine the optimal procedure for the Cape Sorell quartzite preparation, and in this case the liquid nitrogen was chosen as it had been shown to cause less porosity, thus presumably reducing the risk of breaking the samples that had already undergone time-consuming precision grinding. Heating to 1100°C prior to quenching resulted in decomposition of the accessory muscovite. Mercury porosimetry later confirmed that this treatment of the Cape Sorell quartzite increased the porosity of the sample to 2.3%, and inspection of the thin sections confirmed that both intergrain and intragrain cracks (Figure 2b) were created during the treatment.

Thin section images show that, in both cases, the treatments caused significant cracking of the specimens (Figures 2 and 3) while achieving a relatively isotropic crack distribution with reasonably random crack orientation. Mercury porosimetry and SEM images show that the low aspect ratio cracks demonstrate little variation in size, with a distribution of pore throat sizes centered around 0.4 μm and 0.7 μm, respectively, for the Alberta and Cape Sorell samples (Figure 4). Mercury porosimetry of a separate uncracked Alberta quartzite sample shows that this is an increase from an initial pore throat size of 0.1 μm. No measurements were possible on uncracked Cape Sorell quartzite due to a lack of sample availability.

3. Measurement Method

3.1. High-Frequency Measurements

High-frequency measurements were made with the conventional ultrasonic pulse transmission method using 1 MHz piezoelectric ceramics. The measurements were made under differing saturation states that included dry, argon saturated, and water saturated (Tables S1–S6). Piezoelectric transducers capable of generating 1 MHz *P* and *S* waves were affixed to aluminum buffers; the quartzite samples were placed in between the buffers and encased in flexible tubing. They were then subjected to confining pressure only for the dry measurements and independently controlled confining and pore pressure for the argon and water-saturated measurements.

Pore fluid was introduced through a small diameter hole in the topmost buffer and allowed to equilibrate prior to the shear modulus measurements. The allocated equilibration time increased from a minimum of 10 min at 10 MPa of effective pressure to a minimum of 1 h by 50 MPa; >3 h of time was typically allocated at pressures >100 MPa, with some equilibration times of up to 12 h during overnight periods in the multiday measurement process. In order to calculate the high-frequency shear modulus, the *S* wave travel time through the sample and buffers was measured at a series of effective pressures. The travel time through the quartzite sample alone, t_s, was determined by measuring the travel time through the two buffers when no sample was present and subtracting that from the overall time (Molyneux & Schmitt, 2000). Pressure effects on the buffers were removed by measuring the buffers over the same range of pressures as the buffer and sample combination. *S* wave travel time was used in conjunction with the sample bulk density to obtain the high-frequency shear modulus:

$$\mu_H(P_{\text{eff}}) = \left[\frac{l}{t_s(P_{\text{eff}})}\right]^2 \rho, \tag{1}$$

where μ_H is the high-frequency shear modulus, l the sample length, ρ the bulk density, and P_{eff} the effective

pressure. For these measurements, the quartzites had sample lengths of 3 cm. Volumetric changes of the frame between 0 and 150 MPa were estimated using the isothermal bulk modulus and pressure derivative values of single crystal quartz (Liu, 1993) as input into the Birch-Murnaghan equation of state (Birch, 1947). The effect of these volumetric changes on the samples' bulk densities and lengths was calculated. The *P* wave velocities were simultaneously measured at high frequency across a similar range of pressures; the results from the *P* wave measurements will be presented in a forthcoming paper.

Dry measurements were made after the samples were dried overnight in a vacuum oven and then left at ambient conditions and humidity for several days in an effort to avoid artifacts from being "overdried" (Cadoret, 1993). Argon-saturated measurements were made next, over Terzhagi effective pressures from 10 to 150 MPa. For safety reasons, it was not possible to pressurize the argon pore fluid beyond 10 MPa during the high-frequency measurements, so the desired effective pressures were obtained by keeping the argon pore pressure at 10 MPa and varying the confining pressure, as necessary. Water-saturated measurements were made after saturating the sample with distilled water overnight at a Terzhagi effective pressure < 5 MPa. During water-saturated measurements, the confining pressure was kept constant at 150 MPa while the pore pressure was varied to obtain the appropriate range of effective pressures. Travel time picks were difficult to make accurately at lower effective pressures when the samples were dry or argon saturated due to high attenuation of the signal (Li et al., 2014; Figure 3). In the most difficult cases, at 10 or 20 MPa of effective pressure, cross correlation was required to determine a travel time pick. In all cases, care was taken to quantify the uncertainty in the travel time picks as accurately as possible.

3.2. Low-Frequency Measurements

Low-frequency measurements (0.01–1 Hz, with additional, limited, 0.001–0.01 Hz measurements) were made using the specific samples used for 1 MHz measurement, although adjustments to the sample lengths were required (due to signal-to-noise limitations) in order to move between the techniques. Measurements were completed using the Australian National University forced oscillation apparatus. The apparatus is unique, and a more detailed description, including representative examples of raw data, can be found in Jackson and Paterson (1993) and Jackson et al. (1984). The apparatus consists of a long, thin beam that is cantilevered at one end and essentially free at the other, where it is harmonically twisted by a pair of opposing electromagnetic drivers. The cylindrical core sample (a standard sample size of 15 mm diameter $\times$ 150 mm length is used for the apparatus), sandwiched between two polycrystalline (Duramic) alumina rods and encased in a 0.5 mm thick annealed copper jacket, was placed in the top of the apparatus, above a hollow steel elastic standard. To achieve the required 150 mm total sample length, three 50 mm long pieces of the Cape Sorell quartzite were stacked and frictionally coupled together, while the original rock sample of the Alberta quartzite was large enough to allow a single 150 mm long piece to be machined. The beam was sinusoidally driven by a pair of electromagnetic drivers at its base, and torsional mode displacements were measured at two locations along the beam: one immediately below the sample, but above the elastic standard, and one below both the sample and the elastic standard. Measurements of the angular displacement caused by the applied torque from the electromagnetic drivers were made using parallel plate capacitors mounted at the end of lever arms for mechanical advantage (Figure 5). Shear modulus of the sample is inferred by a comparison with a parallel experiment with identical geometry, pressure, and pore fluid conditions in a purely elastic control specimen of known modulus.

The apparatus is capable of applying confining and pore pressure independently to the sample and was recently modified to allow condensed fluids such as water to be used as a pore fluid, in addition to argon gas (Jackson et al., 2011). Pore fluid is introduced into the sample from upper and lower pore fluid reservoirs through the 2 mm diameter bore of each of the hollow polycrystalline alumina rods sandwiching the sample. The pressure of the upper and lower pore fluid reservoirs can be adjusted independently, and when the pressure is increased or decreased in one of the pore fluid reservoirs, the change in pressure with time of the other reservoir can be monitored to measure permeability within the sample using the transient flow method.

The samples were prepared for low-frequency measurement in a manner similar to the preparation for the high-frequency measurements, with the samples vacuum oven dried and then equilibrated at ambient conditions prior to measurement. For the low-frequency measurements the Terzhagi effective pressure was varied by changing the pore fluid pressure at constant high confining pressure.

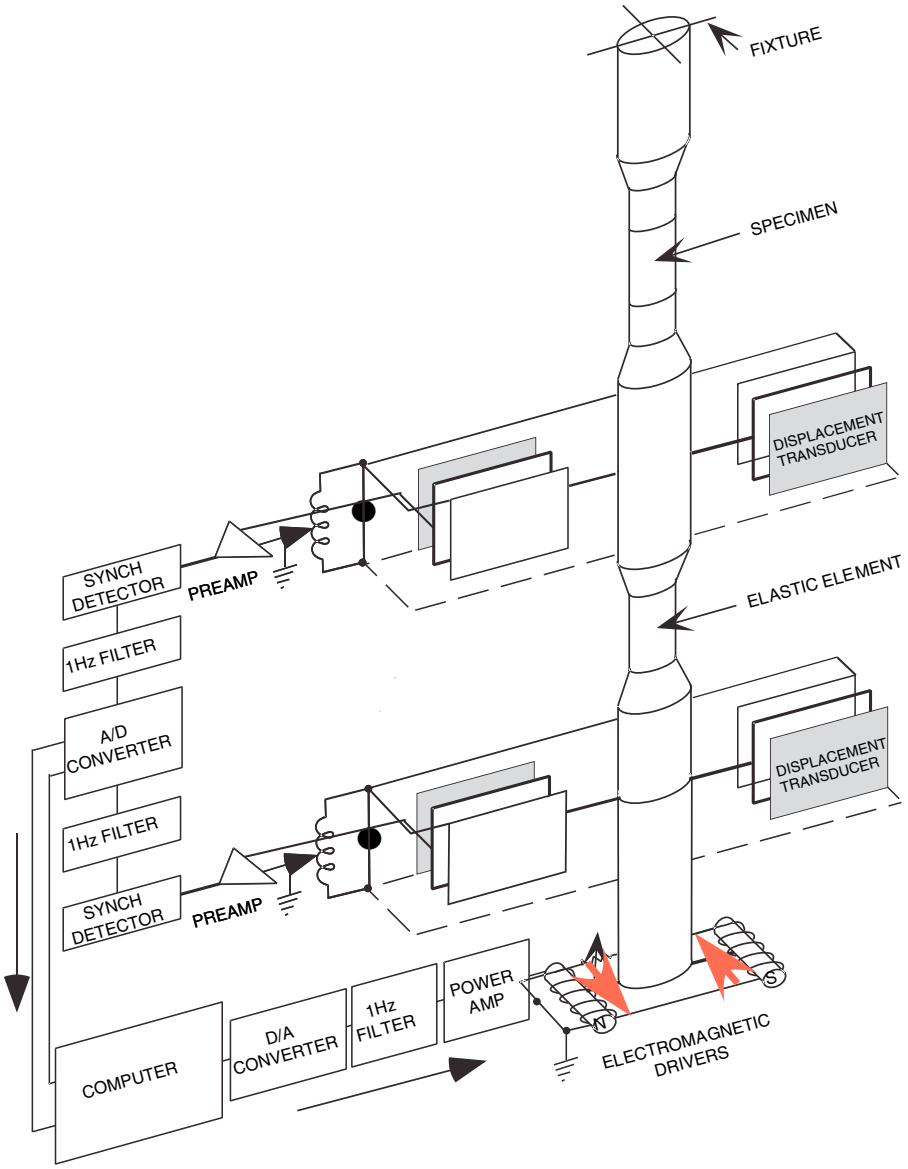

Figure 5. Diagram of ANU attenuation apparatus used to make low-frequency measurements (modified from Jackson et al., 2011).

3.3. Permeability Measurements

In principle, when a state of uniform fluid pressure, P_0, is established throughout the upper and lower pore pressure reservoirs of the apparatus for low-frequency measurement as well as the sample, the permeability, κ, and storage capacity of the sample can be measured by perturbing the system by a small pressure increment, ΔP, in the upper reservoir and measuring the decay or growth of pressure (Neuzil et al., 1981). In the case of the quartzites, however, the storage capacity of the samples themselves is sufficiently small compared to the capacity of the upper and lower pore pressure reservoirs, S_u and S_d, that it is possible to obtain the permeability using the approximation of Hsieh et al. (1981) for negligible storage capacity (Lu & Jackson, 2006):

$$\frac{(P(t)-P_0)}{\Delta P}=\frac{[S_u+S_d\ \ \exp(-At)]}{S_u+S_d} \tag{2}$$

where the rate constant is given by:

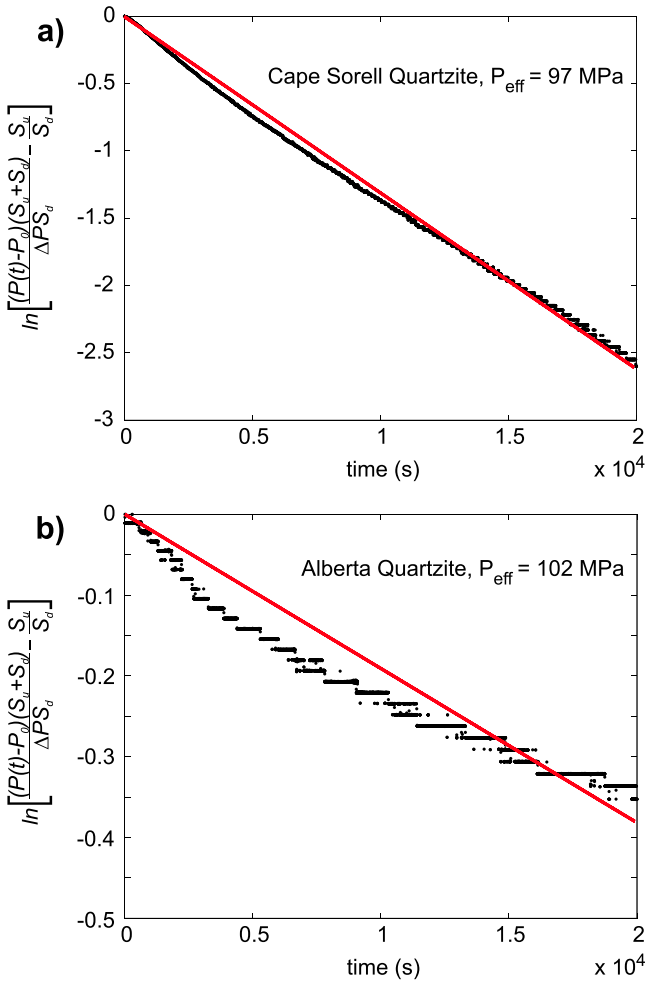

Figure 6. Pore pressure reequilibration (equation (4)) data for the Cape Sorell (a) and Alberta (b) quartzites at ~100 MPa of effective pressure. Note that panels (a) and (b) record >90% and only ~30% of full pore pressure reequilibration during 20,000 s, with time constants A^{-1} of 2 and 15 h, respectively. Measurements of the low permeability (1.2×10^{-21} m^2 at this pressure) of the Alberta quartzite are approaching the resolution limit of the pore pressure transducers.

$$A = \frac{\kappa A_s}{\eta L_S S_u}\left(1 + \frac{S_u}{S_d}\right) \tag{3}$$

Here A_s is the cross-sectional area of the sample, L_s is the sample length, $P(t)$ is the upper reservoir pressure, and η is the fluid viscosity. As the equation assumes that the fluid properties are constant over the induced pressure gradient, permeability measurements are made when the quartzites are saturated with water rather than argon. Over the pressure increments used the physical properties of water show very little change and an approximation of constant properties is reasonable. Equation (2) can be rearranged to

$$\ln\left[\frac{(P(t) - P_0)(S_u + S_d)}{\Delta P S_d} - \frac{S_u}{S_d}\right] = -At \tag{4}$$

The pressure data are plotted as per equation (4); assuming the equation acts, the slope of the resulting line ($-A$) allows permeability k to be solved for through the rearrangement of equation (3). The inverse of the rate constant, that is, A^{-1}, is the time constant for the exponential decay of the pore pressure perturbation, being the time required for the perturbation to decrease to 1/e times its initial value.

Measurements were made by first collapsing the annealed copper jacket enclosing the specimen under high effective pressure. This was done with no pore pressure in the system and confining pressures >80 MPa. This caused the copper jacket to mold closely to the outside of the sample, minimizing any fluid flow at the jacket-specimen boundary. Under confining pressure the lower reservoir, with volume 40,000 mm^3 (Lu, 1996), was then pressurized with water containing a commercial rust inhibitor with both oil and particulate matter in suspension, which was allowed to flow to the upper reservoir (volume 1,163 mm^3) until the pressures in each reservoir equilibrated and the specimen was fully saturated. Pressure measurements in each reservoir were made using high-pressure transducers (Precise Sensors, model 114) with a resolution of 0.1 mV/10 V, which were calibrated against a Bourdon-tube (Heise) pressure gauge. In practice, this resulted in a resolution of about 0.05/500 MPa. The data were recorded digitally using LabView software (National Instruments) and a multichannel acquisition card. Permeability measurements were then taken by changing the pore pressure in the upper reservoir and monitoring the growth or decay of pressure. In cases of extremely low permeability, it was sometimes necessary to adjust the pressure in the upper or lower reservoir during such reequilibration in order to reduce otherwise excessive delay in achieving pore pressure equilibrium at appropriate final effective pressures for the shear modulus measurements; in these instances, the data during and after this midmeasurement adjustment were not used in determining the permeability, reducing the overall measurement time. A least squares fit, constrained to pass through the origin, over the time from the initial adjustment until either equilibrium was reached or the pressures were further manually adjusted, was applied to the data, and the permeability was calculated (Figure 6).

Measuring the timescale of pressure equilibration between the two reservoirs by fluid flow through the sample served the dual purpose of allowing a measurement of permeability and ensuring that pore pressure within the sample was equilibrated prior to the commencement of forced oscillation measurements, although full equilibration of pore pressure throughout the specimen may not have been achieved at the lowest permeabilities. Further, the required equilibration time was used as a guide to ensure that pore pressure was constant throughout the sample prior to the acquisition of the high-frequency measurements as well.

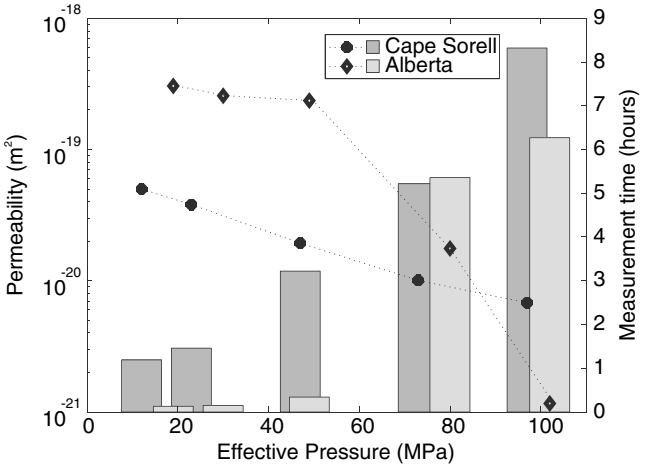

Figure 7. Permeability (dotted lines, left *y* axis) of the Cape Sorell (circles, dark gray bars) and Alberta (diamonds, light gray bars) quartzites as a function of effective pressure, with the experimental measurement time of each data point (bars, right *y* axis).

4. Experimental Results

4.1. Permeability

The pore pressure reequilibration generally adheres to the exponential time dependence prescribed by equation (4) (e.g., Figure 6a). However, the apparently systematic diminution of the rate of reequilibration for the Alberta quartzite at the highest differential pressure (Figure 6b) may reflect progressive clogging of narrow throats in the crack network by oil and/or particulate matter in suspension in the rust inhibitor. The permeabilities, measured as outlined in section 3.3 with water as pore fluid, are extremely low for both quartzites, ranging downward with increasing differential pressure from 3×10^{-19} m^2 to 1×10^{-21} m^2 (Figure 7). The associated time constants range from 15 min at low effective pressures to 15 h for the Alberta quartzite at the highest differential pressure, ~100 MPa. A more moderate maximum of 2 h was measured for the Cape Sorell quartzite, but both samples were allowed overnight equilibration of pore pressure at the higher pressures prior to measurement of shear moduli and wave speeds.

The Cape Sorell quartzite showed a well-behaved exponential decrease in permeability with increased effective pressure. The Alberta quartzite permeability, while still showing a clear decrease with effective pressure, did not demonstrate a straightforward relationship with effective pressure, instead undergoing a sharp decrease in permeability at effective pressures greater than 50 MPa. This may be as a result in a difference in how the measurements were made or may be an actual effect in the rock. The Cape Sorell measurements were made at nearly constant confining pressure (varying from 139 to 140 MPa) with the variation in effective pressure being achieved by change in pore pressure. Time constraints during efforts to obtain the desired final pore pressure in the Alberta quartzite meant that, to avoid unnecessary delay while waiting for complete pore pressure equilibration, adjustments to the pore pressure in the middle of the equilibration process were made more frequently, with the result that some of the permeability measurements on the Alberta quartzite were obtained over a shorter time frame than the equivalent measurements on the Cape Sorell quartzite.

The effective permeability measured on the Alberta quartzite does appear to show some dependence on measurement interval (Figure 6b), with higher apparent permeability at early times. The length of measurement may account for some of the higher permeability seen in the Alberta quartzite at low effective pressures during short measurements (Figure 7); however, it likely does not completely explain the significant permeability decrease beyond 50 MPa of pressure and is addressed further in the discussion.

4.2. Shear Moduli

4.2.1. Crack Closure

Measurements of the dry shear moduli of both quartzites show the shear moduli increasing systematically with effective pressure as the cracks in the samples undergo progressive closure. This effect is quite strong, with the modulus of the dry Alberta quartzite increasing from 11.9 ± 0.3 GPa to 34.9 ± 0.1 GPa over confining pressures 10–150 MPa at high frequency: an increase of 193%. Similarly, the shear modulus of the dry Cape Sorell quartzite increases from 11 ± 1 GPa to 36.0 ± 0.1 GPa from 10 to 130 MPa confining pressure (Figure 8). The quartzites both exhibit substantial increases in their shear moduli continuing to the highest effective pressures but with diminishing pressure sensitivity beyond ~80 MPa.

4.2.2. Dry Conditions

The dry Cape Sorell quartzite, as expected, does not exhibit any shear modulus dispersion, with consistent shear modulus measurements observed from 0.01 Hz to 1 MHz (Figure 9). Low-frequency measurements were made on the Alberta quartzite only under water-saturated conditions, and hence, no dry or argon-saturated results are available in this frequency band.

4.2.3. Effects of Argon Saturation

At low frequencies, argon saturation does not affect the Cape Sorell shear moduli, which are similar to those measured under dry conditions. At 1 MHz, the effect of argon saturation on the Cape Sorell quartzite is a modest, but systematic, increase in the shear moduli—by as much as 24% at 10 MPa, from 11 ± 1 GPa

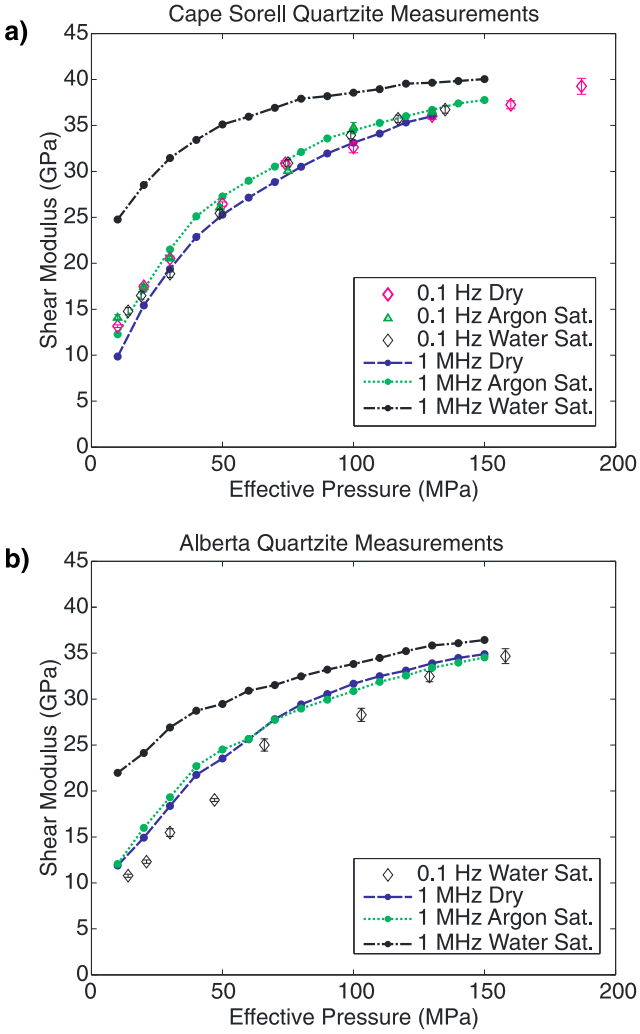

Figure 8. Shear moduli of the Cape Sorell (a) and Alberta (b) quartzites as a function of effective pressure at 0.1 Hz and 1 MHz when dry, water, or argon saturated.

when dry to 12.3 ± 0.4 GPa when argon saturated. For the Alberta quartzite, effects of argon saturation are barely resolvable. Where effects greater than the experimental error can be observed, a maximum increase of 7%, from 14.9 ± 0.1 GPa when dry to 16.0 ± 0.1 GPa when saturated, can be observed at 20 MPa of pressure. At pressures >60 MPa this effect reverses, with a decrease of approximately 1% observed.

4.2.4. Effects of Water Saturation

At 1 MHz the effects of water saturation on the shear moduli are dramatic (Figure 8). The largest effects are measured at the lowest effective pressure, 10 MPa, where water saturation causes the shear modulus of the Alberta quartzite to increase by 85% to 22.0 ± 0.2 GPa and that of the Cape Sorell quartzite to increase by 127% to 24.7 ± 0.1 GPa (Figures 9 and 10).

In marked contrast with the results at 1 MHz, measurements made at frequencies of 0.01–1 Hz, and where available as low as 0.001 Hz, indicate that fluid saturation causes no significant increase of the shear moduli of the quartzites across this frequency range. The more definitive results of fluid effects were obtained on the Cape Sorell quartzite which, unlike the Alberta quartzite, was tested at low frequencies under dry, argon-saturated, and water-saturated conditions. Moreover, the forced-oscillation measurements indicate frequency independence between 1 mHz and 1 Hz.

Taken together, the results thus demonstrate strong dispersion between 1 Hz and 1 MHz—especially for water saturation (Figures 9 and 10).

5. Modeling

5.1. Modulus Deficit and Crack Density

Numerous models quantify the effect of dry and saturated cracks on shear moduli. The popular models require various inputs; as an example, the Biot (1956) model requires an estimate of the permeability of the rock, the pore dimensions, and the tortuosity. Here a perturbation model is chosen for its focus on crack-related effects and for its relative simplicity, requiring only the crack density and the elastic parameters of the uncracked rock. For a dilute concentration of randomly oriented cracks, the shear modulus of a dry cracked medium, μ_{dry}, is given to first order as

$$\frac{\mu_{dry}}{\mu_0} = 1 - \frac{16}{45}\varepsilon\left[\frac{(\lambda_0 + 2\mu_0)(9\lambda_0 + 10\mu_0)}{(3\lambda_0 + 4\mu_0)(\lambda_0 + \mu_0)}\right] \quad (5)$$

(Hudson, 1981; O'Connell & Budiansky, 1974; Walsh, 1969). λ_0 and μ_0 are the Lamé parameters of the nonporous, uncracked rock and the crack density, ε, is defined as

$$\varepsilon = Na^3 \quad (6)$$

Here N is the number density (i.e., number of cracks per unit volume) and a the crack radius. Note that in this approximation, valid for low aspect ratio $\alpha = c/a << 1$, the modulus deficit is a function only of the crack density, ε, rather than both crack porosity and aspect ratio.

When rocks are in the saturated isobaric fluid flow regime, the shear modulus of the saturated rock behaves as when dry (O'Connell & Budiansky, 1977). As a result, equation (5) can be used to calculate the crack densities of both the Cape Sorell and Alberta quartzites using the shear modulus deficits, measured either dry (Cape Sorell) or water saturated (Alberta), and the Lamé parameters of quartz, Hashin-Shtrikman averages of 44.1 GPa and 8.22 GPa (McSkimin et al., 1965) at STP, respectively, for μ_0 and λ_0.

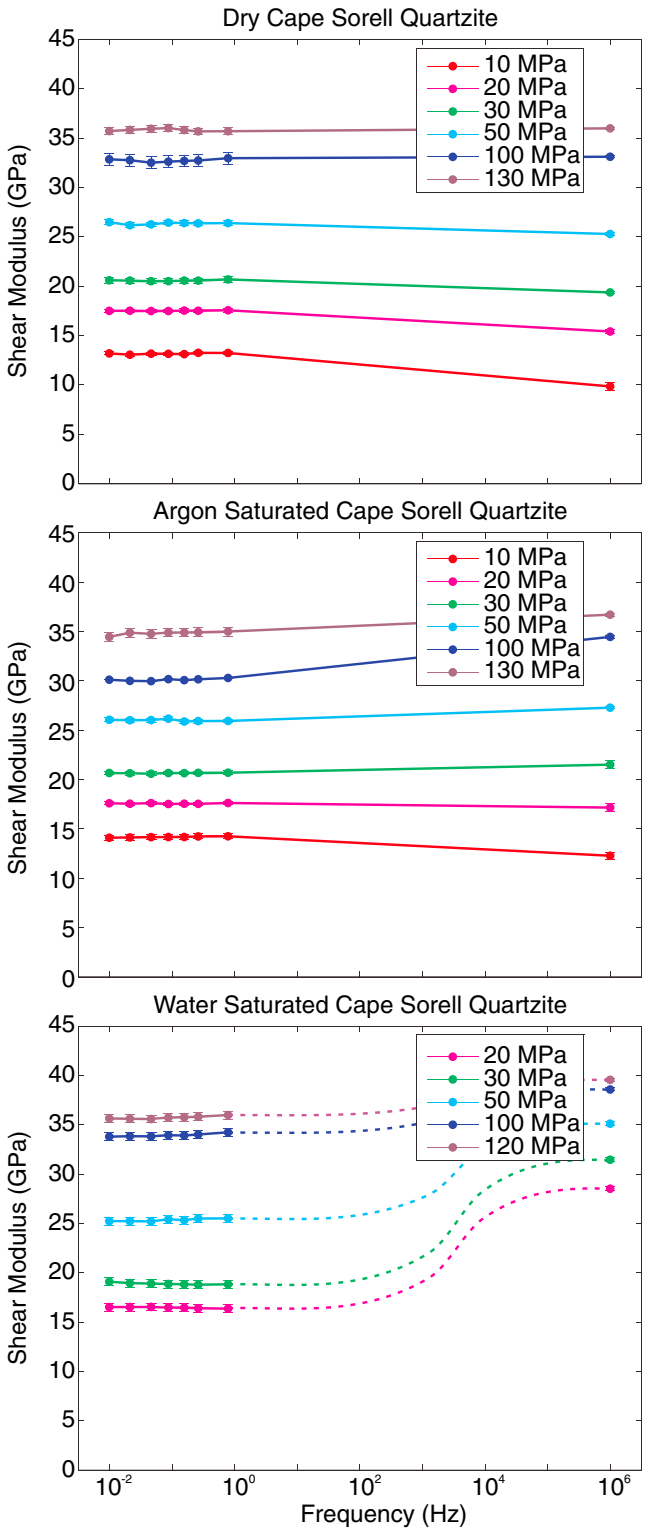

Figure 9. Cape Sorell quartzite shear moduli from 0.01 to 1 Hz and at 1 MHz, at varying pressures, measured dry (top), argon saturated (middle), and water saturated (bottom) during the "up" pressurization cycle. Listed effective pressures are those corresponding to the high-frequency measurement; low-frequency measurements may vary from the pressure listed in the figure by up to 3 MPa.

The crack density ε for the Cape Sorell quartzite is thus inferred to decrease from 0.4 at the lowest differential pressure P_d of 10 MPa to below 0.1 at high pressure; however, the pressure sensitivity of the inferred crack density decreases with increasing pressure especially for the Cape Sorell quartzite. The crack density for the Alberta quartzite is higher than that of the Cape Sorell quartzite by ~ 0.05 throughout the measurement range and appears to still be moderately decreasing below 0.15 at the highest effective pressure of 158 MPa (Figure 11).

Broadly similar results were obtained by Li et al. (2014), using a more elaborate differential effective medium model for material containing both cracks and unclosable pores. The authors inferred a crack density for the same cracked Cape Sorell quartzite of ~ 0.5 for P_{eff} = 20 MPa decreasing to $<$0.1 for $P_{\text{eff}} > 80$ MPa.

5.2. Pressure-Induced Crack Closure and Crack Aspect Ratio

The shear moduli at even the highest pressures measured remain lower than the Hashin-Shtrikman average of 44.1 GPa calculated from single crystal quartz (McSkimin et al., 1965), and it is inferred that the quartzites retain finite porosity even at pressures $>$150 MPa. For all measurements, however, the shear moduli appear to enter a more linear regime at ~80 MPa of effective pressure, indicating that many of the cracks reach maximum effective closure around this pressure. Walsh (1965) gives the effective confining pressure needed to close a randomly oriented penny-shaped crack as

$$P_{\text{eff}} = \frac{\pi\alpha\mu_0}{2(1-\nu_0)} \tag{7}$$

where ν_0 is the mineral Poisson ratio. For a pressure of 80 MPa, representative of the broad regime of inferred crack closure, equation (7) can be solved for an initial value of α. Using the previously mentioned shear modulus for quartz and the Poisson ratio, 0.078, calculated from the Hashin-Shtrikman average bulk modulus value of 37.7 GPa (McSkimin et al., 1965) yields a zero-pressure aspect ratio of 0.001. As crack closure occurs over a range of pressures both lower and higher than 80 MPa, there must in fact be a distribution of aspect ratios, centered around 0.001 as inferred by Li et al. (2014). An aspect ratio of 0.001, combined with throat sizes of Figure 4, corresponds to crack diameters of 0.4 mm for the Cape Sorell quartzite and 0.7 mm for the Canadian quartzite, comparable with the grain sizes (both ~0.5 mm) of both which can be expected to form an upper limit on crack size.

5.3. Characteristic Frequencies

Such a representative zero-pressure aspect ratio may be used to provide an indicative value of the characteristic frequency separating the saturated isolated (squirt flow) and saturated isobaric fluid flow regimes, $f \sim K\alpha^3/2\pi\eta$ (O'Connell & Budiansky, 1977), where K is the bulk modulus of the medium and η the fluid viscosity. The aspect ratio, and hence the characteristic frequency, may have some pressure dependence, but accurate analysis of this is somewhat elusive and hence a constant aspect ratio is assumed. The existence of a distribution of aspect ratios will inevitably broaden the transition

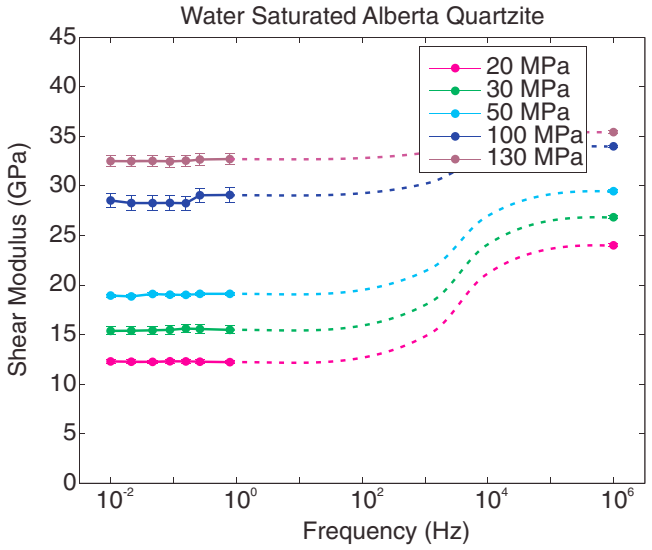

Figure 10. Water-saturated Alberta quartzite shear modulus measurements from 0.01 to 1 Hz and at 1 MHz, measured during the up pressurization cycle. Listed effective pressures are those corresponding to the high-frequency measurement; low-frequency measurements may vary from the pressure listed in the figure by up to 3 MPa.

between fluid flow regimes around the estimated characteristic frequency.

For water, with a viscosity of 1 mPa s at STP, a characteristic frequency of ~6 kHz is calculated for the water-saturated quartzites, clearly separating the low-frequency, 0.1–1 Hz, and high-frequency, 1 MHz, measurements into the saturated isobaric and saturated isolated fluid flow regimes, respectively. At 10 MPa, argon has a viscosity of only 0.03 mPa s, resulting in a significantly higher characteristic frequency of ~0.2 MHz for squirt flow—but consistent with MHz measurements probing the saturated isolated regime.

At long measurement times an additional fluid flow regime exists, the "drained" regime. This regime is characterized by stress-induced fluid exchange between the pore space and an external reservoir. The characteristic frequency, $f \sim 4\kappa K/L^2\eta$, separates the drained and saturated isobaric regimes, where L is the characteristic length, but the shear modulus is expected to be unaffected by this transition (Cleary, 1978). It is thus estimated that the Alberta quartzite transitions at a frequency as high as ~1 mHz when water saturated and ~10 mHz when argon saturated. The draining transition may occur at even lower frequencies if the pore compressibility of the cracked medium exceeds the fluid compressibility, as for water saturation of cracks of low aspect ratio. As a result of the high pore pressure used for the low-frequency measurements the viscosities of water and argon are closer than in the previous case, reducing the differences between the characteristic frequency calculated for the different saturating fluids. The argon and water-saturated characteristic frequencies of the Cape Sorell quartzite are estimated to have a maximum an order of magnitude lower than their Alberta quartzite counterparts due to the lower permeability of the Cape Sorell quartzite at low pressure.

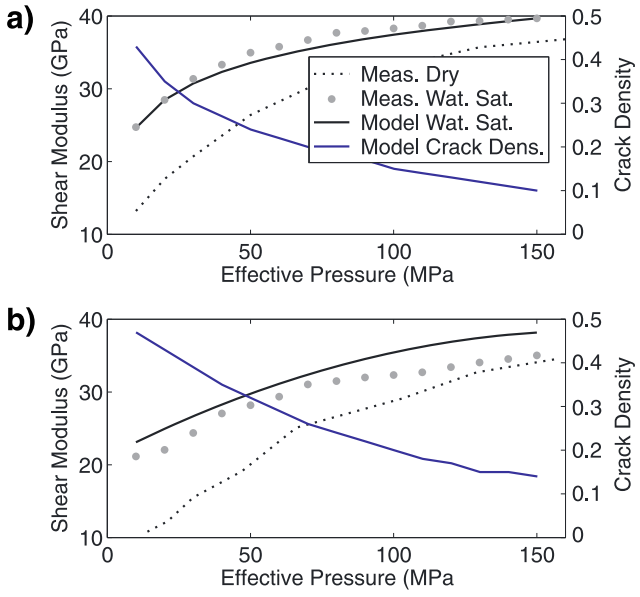

Figure 11. 1 MHz measurements of dry and water-saturated Cape Sorell (a) and Alberta (b) quartzite shear moduli, with a comparison to the Walsh-Hudson estimation of crack density and Walsh-Hudson predictions of water-saturated shear moduli for the respective quartzites within the saturated isolated fluid flow regime.

5.4. Modeling the Effect of Fluid Saturation

Isolated inclusions of low aspect ratio $\alpha << 1$ filled by a moderately incompressible fluid (such that $K_f >> \alpha K_0$) result in a perturbation of the shear modulus (c.f. equation (5)), μ_{sat}, that is a function only of the crack density:

$$\mu_{sat} = -\frac{32}{15}\mu_0\varepsilon\left[\frac{\lambda_0 + 2\mu_0}{3\lambda_0 + 4\mu_0}\right] + \mu_0, \tag{8}$$

(Walsh, 1969, O'Connell & Budiansky, 1974; Hudson, 1981, equations (19) and (37)). As the characteristic frequency calculations indicate that the water-saturated quartzites are in the saturated isolated fluid flow regime during the MHz measurements, the pressure-dependent crack density previously inferred from the "dry" modulus can be used in equation (8) to estimate the saturated shear modulus μ_{sat} of the cracked medium. Accordingly, we calculate the expected effects of water saturation (bulk modulus ~3 GPa at the experimental pressures and temperatures) on the shear moduli of the quartzites. On account of the much lower bulk modulus for argon (e.g., ~10 MPa at P_{fl} = 10 MPa), along with conditions only marginally within the saturated isolated regime, no such modeling of the argon-saturated quartzites was undertaken.

The water-saturated model results show excellent agreement with the experimentally measured results for both the Cape Sorell and Alberta quartzites, indicating that use of the model for both dry and water-saturated conditions effectively captures the dominant effects of fluid on the cracked rocks (Figure 11). This is somewhat surprising, especially for the Alberta quartzite, as the difference between the low-frequency

water-saturated shear moduli and the high-frequency dry moduli introduces uncertainty into the calculation of crack density.

6. Discussion

6.1. Permeability

The Cape Sorell and Alberta quartzites share relatively similar physical properties; both have a largely monominerallic quartz composition, grain sizes of approximately 0.5 mm, total porosities on the order of ~2%, and pore throat sizes <1 μm. Interestingly, however, their permeabilities differ somewhat in behavior. While the Cape Sorell quartzite shows a well-behaved exponential decrease in permeability with increasing effective pressure, the Alberta quartzite shows a sharp decline in permeability at effective pressures >50 MPa. As described earlier, some of this variation may result from differences in the measurement methodology. Part of the variation, however, is expected to be caused by mineralogical differences between the samples. The Alberta quartzite is seen to have smooth grain boundaries, perhaps allowing more complete closure of the intercrack space at high pressure, while the Cape Sorell quartzite has phyllosilicates at the grain boundaries, the thermal decomposition products of which may have acted to hold the intercrack pathways open, even at very high effective pressures.

Overall permeability is somewhat lower than anticipated. This may be the result of oil and particulate matter, in suspension within the commercial rust inhibitor used during water-saturated low-frequency measurements, clogging the pore throats and reducing the rate of fluid flow, and potential chemical interactions between the polar water molecules and the siliceous crack surfaces.

6.2. Crack Properties

The modeled crack densities, >0.4 at low pressures, show that quite high crack densities are possible even in structurally intact rocks. The modeled crack density is, however, insufficient to account for more than ~10% of the total porosity of the samples at the estimated aspect ratio of 0.001. It is concluded that much of the porosity measured at ambient conditions on the thermally cracked quartzites is probably contributed by uniform partings of near-zero aspect ratio (Figures 2d and 3d) expected to close at pressures $<<10$ MPa; cracks of significantly larger aspect ratio than 0.001 that remain open at the highest experimentally accessible pressure of 150 MPa, and account for the residual crack density, also contribute to the total porosity. Previous studies infer the Cape Sorell quartzite to have porosity with an initial aspect ratio of 0.02 (Lu & Jackson, 1998), which may remain an upper bound on the aspect ratio distribution for this quartzite after induced cracking. The larger crack density modeled in the Alberta quartzite than in the Cape Sorell quartzite at high pressures implies that the Alberta quartzite may have either a larger number or more equant, higher aspect ratio, cracks than the Cape Sorell sample.

While we hypothesize the closure of a main population of cracks in both quartzites at ~80 MPa, as the final shear moduli do not reach the value of single crystal quartz, it appears that complete closure of all cracks is not achieved in either quartzite, even at pressures >150 MPa. This is consistent with the observation of modulus deficits relative to predictions from single-crystal elasticity commonly persisting to pressures of order 1 GPa (Christensen, 1974).

6.3. Dispersion

In most ways, the shear moduli of the quartzites behaved similarly. As expected, no significant difference is seen between the low-frequency and high-frequency dry shear moduli measurements, which were completed on the Cape Sorell quartzite alone.

At low frequencies between 0.01 and 1 Hz, the shear moduli show no sensitivity to fluid saturation for either quartzite (Figures 9 and 10). Although the argon-saturated Alberta quartzite approaches the transition to the drained regime, estimated at ~0.01 Hz due to the lower viscosity of argon and higher permeability of this quartzite at low pressure, its shear moduli are consistent across the entirety of the 0.01–1 Hz bandwidth. If the quartzite is indeed approaching or crossing the transition, it must, as is theoretically predicted (e.g., Cleary, 1978), not affect the shear modulus. The assumption that the quartzite can be treated as in the saturated isobaric regime therefore appears valid.

Gassmann (1951) predicts that the dry and saturated shear modulus of a rock will be equal when the rock is in a saturated isobaric fluid flow regime, and the lack of observed difference between the saturated and dry states for Cape Sorell quartzite supports that the low frequencies measured here, 0.01–1 Hz, are sufficiently low to allow pore pressure equilibration during the course of the measurement. The bulk density of the sample increases negligibly with saturation due to the low porosity of the samples, with the result that fluid saturation has no significant effect on shear wave velocities.

Water saturation causes strong dispersion, evident in the markedly increased shear moduli of both quartzite specimens at 1 MHz when compared to 1 Hz (Figure 8). The measured dispersion requires a transition in fluid flow regimes between 1 Hz and 1 MHz. The estimated frequency for squirt flow places the saturated isobaric-saturated isolated boundary near kilohertz frequencies for water saturation in these rocks, indicating that the 1 MHz measurements probe the saturated isolated regime. The magnitude of dispersion between 1 Hz and 1 MHz is most pronounced at lower effective pressures when the cracks are open and crack density is higher. Interestingly, at these pressures the magnitude of dispersion observed is similar to that indirectly measured in Fontainebleau sandstone by Pimienta et al. (2015) at low pressure (1 MPa), despite the sandstone being reported to have significantly higher porosity (7.3%) and more equant pores. At pressures $>$80 MPa, beyond which the majority of the cracks are closed, the differences between the water-saturated and dry or argon-saturated shear moduli are smaller (Figure 8) but still significant. This indicates that, even at the highest effective pressures measured here, some porosity remains, with the cracks having reduced compliance when saturated. Crack density and aspect ratio modeling show that, at high pressure, cracks with higher aspect ratio may still remain open and maintain a crack density as high as 0.1 in both quartzites.

During the argon-saturated 1 MHz measurements, the Cape Sorell quartzite's argon-saturated shear modulus exceeds its dry shear modulus at all measured effective pressures, while this is true only for measurements made from 10 to 50 MPa for the Alberta quartzite. Theoretically, the regime transition occurs between 0.2 MHz at low pressures, and it appears likely that this increase results from the argon-saturated samples behaving as in the saturated isolated regime. The slight decrease observed in the Alberta quartzite at higher pressures is difficult to understand and may be explained by preferential closure of low aspect ratio cracks raising the characteristic frequency at high pressures or perhaps additional cracking developing during the pressurization cycle.

7. Conclusions

Each of the two quartzites studied from Cape Sorell, Australia, and Alberta, Canada, contain a population of thermal cracks of low aspect ratio embedded within a near monominerallic quartz frame. Shear modulus dispersion was successfully measured on both samples, providing important experimental results for a field largely dominated by theoretical work. The dry shear modulus of each of the cracked quartzites increases markedly with increasing effective pressure, reflecting the progressive reduction of the initially high-induced crack densities. The crack density, in each case ~0.4 at low pressure, more than halves the shear modulus from its value at high pressure, demonstrating the significant effect cracks, can have on seismic velocities in low-porosity rocks.

No dispersion is observed for the dry quartzites, as expected. The water-saturated quartzites, however, show substantial frequency-dependent dispersion in their shear moduli, with the 0.01–1 Hz measurements in the saturated isobaric regime and the 1 MHz measurements in the saturated isolated regime. High-frequency water-saturated shear moduli were substantially larger than those measured at low frequencies. At 1 MHz and 20 MPa of effective pressure, the water-saturated shear moduli are almost twice as large as their 1 Hz counterparts: 74% higher for the Cape Sorell quartzite and 98% higher for the Alberta quartzite. These results highlight the need to understand the properties of crystalline rocks and their characteristic fluid flow frequencies when it is considered that ultrasonic measurements used to model seismic survey results in crystalline rock are frequently made on core that may be partially saturated and downhole measurements at sonic frequencies most assuredly are.

The Walsh-Hudson model applied to the shear moduli that measured both dry and water saturated appears to satisfactorily represent the effects of water saturation on the shear moduli of the quartzites. Accordingly, if the fluid flow regime of the rock is known, it may be possible to use theoretical models to adequately predict its high-frequency shear modulus from its low-frequency, or dry, modulus.

The limitations in signal-to-noise levels of the measurement techniques mean that no dispersion is conclusively observed between 1 Hz and 1 MHz in the shear modulus of the argon-saturated quartzite measured here, but a comparison of the 1 MHz argon-saturated ultrasonic measurements to the 1 MHz dry measurements indicates that modest dispersion is likely occurring at an amplitude below the ability of these techniques to resolve quantitatively. The characteristic frequency separating the saturated isobaric and saturated isolated fluid flow regimes is calculated to be ~0.2 MHz, placing 1 MHz measurements of the argon-saturated quartzites proximal to the transition but within the saturated isolated regime. While not conclusive, this is supportive of the accuracy of the characteristic frequency given by O'Connell and Budiansky (1977).

As the shear modulus affects both *P* and *S* wave seismic velocities, the experimental results measured on the two quartzite specimens show that dispersion can have a critical effect on velocity measurements of both body waves, with important implications for seismic acquisition and modeling of cracked crystalline rocks. It is generally thought that the majority of the Earth's crystalline crust has fluid-filled cracks, and these can be expected to cause significant velocity dispersion within the seismic record. This data set provides necessary experimental data with which to constrain and test theoretical models for crack parameter inversion and dispersion-related calculations.

Acknowledgments
The authors gratefully acknowledge technical assistance at the Australian National University by Harri Kokkonen and Hayden Miller and at the University of Alberta by Randy Kofman. The thoughtful reviews by Yves Guéguen and an anonymous reviewer also greatly assisted in shaping the manuscript. The work was funded through NSERC Discovery grants to D. R. S. and grant DP110101830 from the Australian Research Council to I. J. and D. R. S. H. S.'s visit to Canberra was funded by the NSERC Michael Smith Foreign Study Supplement. All shear modulus measurements can be found in the supporting information.

References

Adam, L., Batzle, M., Lewallen, K. T., & van Wijk, K. (2009). Seismic wave attenuation in carbonates. *Journal of Geophysical Research*, *114*, B06208. https://doi.org/10.1029/2008JB005890

Batzle, M. L., Han, D. H., & Hofmann, R. (2006). Fluid mobility and frequency-dependent seismic velocity—Direct measurements. *Geophysics*, *71*(1), N1–N9. https://doi.org/10.1190/1.2159053

Biot, M. A. (1956). Theory of propagation of elastic wave in a fluid-saturated porous solid I. Low frequency range II. Higher frequency range. *Journal of the Acoustical Society of America*, *28*(2), 168–191.

Birch, F. (1947). Finite elastic strain of cubic crystals. *Physical Review*, *71*(11), 809–824. https://doi.org/10.1103/PhysRev.71.809

Cadoret, T. (1993). Effet de la Saturation Eau/Gaz sur les Propriétés Acoustiques des Roches, University of Paris, VII.

Chan, J., & Schmitt, D. R. (2015). Examining the in situ metamorphic rock in northeastern Alberta using zero-offset VSP. *International Journal of Earth Sciences (Geol Rundsch)*, *104*, 1549–1562. https://doi.org/10.1007/s00531-014-1110-x

Christensen, N. I. (1974). Compressional wave velocities in possible mantle rocks to pressures of 30 kilobars. *Journal of Geophysical Research*, *79*, 407–412.

Cleary, M. (1978). Elastic and dynamic response regimes of fluid-impregnated solids with diverse microstructures. *International Journal of Solids and Structures*, *14*, 795–819.

Gassmann, F. (1951). Uber die elastizitat pososer medien. *Vier. der Natur. Gesellschaft*, *96*, 1–23.

Hajnal, Z., White, D. J., Takacs, E., Gyorfi, I., Annesley, I. R., Wood, G., et al. (2010). Application of modern 2-D and 3-D seismic-reflection techniques for uranium exploration in the Athabasca Basin. *Canadian Journal of Earth Sciences*, *47*(5), 761–782. https://doi.org/10.1139/e10-026

Heinonen, S., Heikkinen, P. J., Kousa, J., Kukkonen, L. T., & Snyder, D. B. (2013). Enhancing hardrock seismic images: Reprocessing of high resolution seismic reflection data from Vihanti, Finland. *Journal of Applied Geophysics*, *93*, 1–11. https://doi.org/10.1016/j.jappgeo.2013.03.004

Hsieh, P. A., Tracy, J. V., Neuzil, C. E., Bredehoeft, J. D., & Silliman, S. E. (1981). A transient laboratory method for determining the hydraulic properties of 'tight' rocks—I. Theory. *International Journal of Rock Mechanics and Mining Sciences*, *18*(3), 245–252. https://doi.org/10.1016/0148-9062(81)90979-7

Hudson, J. A. (1981). Wave speeds and attenuation of elastic-waves in material containing cracks. *Geophysical Journal of the Royal Astronomical Society*, *64*(1), 133–150.

Jackson, I., & Paterson, M. S. (1993). A high-pressure, high-temperature apparatus for studies of seismic-wave dispersion and attenuation. *Pure and Applied Geophysics*, *141*(2–4), 445–466.

Jackson, I., Paterson, M. S., Niesler, H., & Waterford, R. M. (1984). Rock anelasticity measurements at high-pressure, low strain amplitude and seismic frequency. *Geophysical Research Letters*, *11*, 1235–1238.

Jackson, I., Schijns, H., Schmitt, D. R., Mu, J. J., & Delmenico, A. (2011). A versatile facility for laboratory studies of viscoelastic and poroelastic behaviour of rocks. *Review of Scientific Instruments*, *82*(6). https://doi.org/10.1063/1.3592154

Koivisto, E., Malehmir, A., Heikkinen, P., Heinonen, S., & Kukkonen, I. (2012). 2D reflection seismic investigations at the Kevitsa Ni-Cu-PGE deposit, northern Finland. *Geophysics*, *77*(5), WC149–WC162. https://doi.org/10.1190/geo2011-0496.1

Li, Y., Olin, M., David, E. C., Jackson, I., Schijns, H., & Schmitt, D. R. (2014). Broadband laboratory measurements of dispersion in thermally cracked and fluid-saturated quartzite and a synthetic analogue. *The Leading Edge*, *33*(6), 624–626. https://doi.org/10.1190/tle33060624.1

Lu, C. (1996). *Shear mode anelasticity of thermally cracked and fluid-saturated rocks*. Australian National University.

Lu, C., & Jackson, I. (1998). Seismic-frequency laboratory measurements of shear mode viscoelasticity in crustal rocks—II: Thermally stressed quartzite and granite. *Pure and Applied Geophysics*, *153*(2–4), 441–473.

Lu, C., & Jackson, I. (2006). Low-frequency seismic properties of thermally cracked and argon-saturated granite. *Geophysics*, *71*(6), F147–F159. https://doi.org/10.1190/1.2345053

Malehmir, A., Juhlin, C., Wijns, C., Urosevic, M., Valasti, P., & Koivisto, E. (2012). 3D reflection seismic imaging for open-pit mine planning and deep exploration in the Kevitsa Ni-Cu-PGE deposit, northern Finland. *Geophysics*, *77*(5), WC95–WC108. https://doi.org/10.1190/geo2011-0468.1

Mallet, C., Fortin, J., Guéguen, Y., & Bouyer, F. (2013). Effective elastic properties of cracked solids: An experimental investigation. *International Journal of Fracture*, *182*(2).

Mavko, G., & Jizba, D. (1991). Estimating grain-scale fluid effects on velocity dispersion in rocks. *Geophysics*, *56*(12), 1940–1949.

McSkimin, H. J., Andreatc, P., & Thurston, R. N. (1965). Elastic moduli of quartz versus hydrostatic pressure at 25° and −195.8°C. *Journal of Applied Physics*, *36*(5), 1624. https://doi.org/10.1063/1.1703099

Milkereit, B., Eaton, D., Wu, J., Perron, G., Salisbury, M., Berrer, E. K., & Morrison, G. (1996). Seismic imaging of massive sulfide deposits.2. Reflection seismic profiling. *Economic Geology and the Bulletin of the Society of Economic Geologists*, *91*(5), 829–834.

Molyneux, J. B., & Schmitt, D. R. (2000). Compressional-wave velocities in attenuating media: A laboratory physical model study. *Geophysics*, *65*(4), 1162–1167. https://doi.org/10.1190/1.1444809

Neuzil, C. E., Cooley, C., Silliman, S. E., Bredehoeft, J. D., & Hsieh, P. A. (1981). A transient laboratory method for determining the hydraulic properties of 'tight' rocks—II. Application. *International Journal of Rock Mechanics and Mining Sciences*, *18*(3), 253–258. https://doi.org/10.1016/0148-9062(81)90980-3

National Institute of Standards and Technology (2012). *NIST standard reference database 203 web thermo tables (WTT)—Professional edition*.

O'Connell, R. J., & Budiansky, B. (1974). Seismic velocities in dry and saturated cracked solids. *Journal of Geophysical Research*, *79*, 5412–5426.

O'Connell, R. J., & Budiansky, B. (1977). Viscoelastic properties of fluid-saturated cracked solids. *Journal of Geophysical Research*, *82*, 5719–5735.

Pimienta, L., Fortin, J., & Gueguen, Y. (2015). Experimental study of Young's modulus dispersion and attenuation in fully saturated sandstones. *Geophysics*, *80*(5), L57–L72. https://doi.org/10.1190/geo2014-0532.1

Schijns, H., Heinonen, S., Schmitt, D. R., Heikkinen, P., & Kukkonen, I. T. (2009). Seismic refraction traveltime inversion for static corrections in a glaciated shield rock environment: A case study. *Geophysical Prospecting*, *57*(6), 997–1008. https://doi.org/10.1111/j.1365-2478.2009.00798.x

Smyth, J. R., & McCormick, T. C. (1995). Crystallographic data for minerals. In T. J. Ahrens (Ed.), *Mineral physics and crystallography. A handbook of physical constants* (pp. 1–17). Washington: American Geophysical Union.

Spencer, J. W. (1981). Stress relaxations at low frequencies in fluid-saturated rocks. *Journal de Physique*, *42*(NC5), 1175–1180.

Spencer, J. W., & Shine, J. (2016). Seismic wave attenuation and modulus dispersion in sandstones. *Geophysics*, *81*(3), D211–D231. https://doi.org/10.1190/geo2015-0342.1

Sun, L. F., Milkereit, B., & Schmitt, D. R. (2009). Measuring velocity dispersion and attenuation in the exploration seismic frequency band.

Tisato, N., & Quintal, B. (2014). Laboratory measurements of seismic attenuation in sandstone: Strain versus fluid saturation effects. *Geophysics*, *79*(5), WB9–WB14. https://doi.org/10.1190/geo2013-0419.1

Walsh, J. B. (1965). Effect of cracks on compressibility of rock. *Journal of Geophysical Research*, *70*, 381–389. https://doi.org/10.1029/JZ070i002p00381

Walsh, J. B. (1969). New analysis of attenuation in partially melted rock. *Journal of Geophysical Research*, *74*, 4333–4337.

White, D. J., & Malinowski, M. (2012). Interpretation of 2D seismic profiles in complex geological terrains: Examples from the Flin Flon mining camp, Canada. *Geophysics*, *77*(5), WC37–WC46. https://doi.org/10.1190/geo2011-0478.1

Winkler, K. W., & Nur, A. (1982). Seismic attenuation—Effects of pore fluids and frictional sliding. *Geophysics*, *47*(1), 1–15.

Yin, C. S., Batzle, M. L., & Smith, B. J. (1992). Effects of partial liquid gas saturation on extensional wave attenuation in Berea sandstone. *Geophysical Research Letters*, *19*, 1399–1402. https://doi.org/10.1029/92GL01159